

Globally Optimal Robust Radar Calibration in Intelligent Transportation Systems

Xinyi Li¹, Yinlong Liu², Venkatnarayanan Lakshminarasimhan¹, Hu Cao¹, Feihu Zhang¹,
and Alois Knoll¹, *Fellow, IEEE*

Abstract—Radar is among the most popular sensors in modern Intelligent Transportation Systems (ITSs), enabling weather-robust perception. The orientation and position of the traffic radar relative to the ITS coordinate system are necessary for the perception fusion in ITSs. However, due to the unknown target association, sparseness and noisiness of traffic radar measurements, the robust and accurate extrinsic calibration of traffic radar is challenging. In this paper, we propose a targetless traffic radar calibration method based on GPS to overcome the inconvenience during ITS operation, because the installation of a dedicated calibration target on the highway is impractical and dangerous. On the other hand, the high-precision GPS device installed on the moving vehicle can provide traffic radar with accurate positioning information of the detection target. Furthermore, during the optimization process of extrinsic calibration, we propose a globally optimal registration method, which is robust to noise and outliers in radar measurements, and is called Gaussian Mixture Robust Branch and Bound (GMRBnB). Specifically, we first construct the robust objective function by utilizing the Gaussian Mixture Model (GMM). Then, we derive novel relaxation bounds and present the GMRBnB algorithm that overcomes the susceptibility to local minima and the dependence on initialization of traditional optimization methods. Compared with existing methods, extensive experiments in synthetic and real-world data demonstrate that our method is not only globally optimal, but also more accurate and robust.

Index Terms—Targetless calibration, traffic radar, intelligent transportation system, Gaussian mixture model, globally optimal, branch and bound.

I. INTRODUCTION

MODERN Intelligent Transportation Systems (ITSs) can significantly improve transportation efficiency and reduce the occurrence of traffic accidents by providing vehicles with extra detailed information about the present traffic flow in

Manuscript received 23 March 2022; revised 19 September 2022; accepted 20 February 2023. This work was supported in part by the Federal Ministry for Digital and Transport, Germany, through the research project Providentia++ under Grant 01MM19008A; and in part by the National Natural Science Foundation of China under Grant 52171322. The Associate Editor for this article was Y. Zhang. (*Corresponding author: Feihu Zhang.*)

Xinyi Li, Venkatnarayanan Lakshminarasimhan, Hu Cao, and Alois Knoll are with the Chair of Robotics, Artificial Intelligence and Real-time Systems, TUM School of Computation, Information and Technology, Technical University of Munich, 85748 Munich, Germany (e-mail: super.xinyi@tum.de; venkat.lakshmi@tum.de; hu.cao@tum.de; knoll@in.tum.de).

Yinlong Liu is with the Faculty of Science and Technology, University of Macau, Macau, China (e-mail: YinlongLiu@um.edu.mo).

Feihu Zhang is with School of Marine Science and Technology, Northwestern Polytechnical University, Xi'an 710072, China (e-mail: feihu.zhang@nwpu.edu.cn).

Digital Object Identifier 10.1109/TITS.2023.3251183



Fig. 1. One of the measurement points on the highway A9 from Providentia++ project (<https://innovation-mobility.com/en/project-providentia/>).

form of a Digital Twin [1], [2]. In ITSs, many heterogeneous sensors, such as monocular cameras, event cameras, Lidars, radars, etc., should be equipped to acquire information on different modalities, as shown in Fig. 1. These sensors, which usually have different capabilities and different fields of view, need to be integrated into the ITS. Extrinsic calibration, a key step in multi-sensor integration, can find the spatial relationship between the sensor coordinate systems and build consistent environment model [3], [4], [5]. Meanwhile, extrinsic calibration is also known as pose estimation or spatial registration [6]. The focus of our investigation is the sensor extrinsic calibration in ITSs.

Traffic radar is known as the most popular sensor for wide application in ITSs, such as object detection, tracking, and localization [7], [8], [9], [10]. Because the millimeter wave can penetrate fog, smoke and dust easily, the millimeter wave radar is robust especially in extreme weather conditions [11], [12]. Moreover, it can detect targets at longer distances than other sensors, such as Lidars. However, the measurements of traffic radar have the following properties:

- Because of the low spatial resolution in the vertical direction, the field of view of the traffic radar is considered to be planar.
- Traffic radar detections are sparse, as shown in Fig. 2. Because the traffic radar outputs measurements solely in the form of detected objects (traffic participants).
- Traffic radar measurements are usually contaminated by noise and outliers, because the reflected waves come from all moving and non-moving targets.



Fig. 2. This is the image after the traffic radar measurements being projected onto the camera picture. The measurements (blue points) are sparse, and contain biases and misdetections caused by noise.

Therefore, due to the low precision and high outlier rate of radar measurements, accurate and robust extrinsic calibration of traffic radar is crucial but challenging. On the other hand, because traffic radar is used to detect and track traffic participants, mainly to confirm which lane they are in, the accuracy of traffic radar calibration is required at the meter level.

Traditional extrinsic calibration methods are generally classified as target-based [13], [14], [15] method and targetless [16], [17], [18] method. Among the target-based methods, researchers leverage external dedicated targets, such as corner reflector, to build reference features for detection and association. However, target-based calibration methods are infeasible for the real practical scenario, such as during ITS operation. Because the installation of dedicated calibration targets on the highway is impractical and dangerous. In addition, it is not always practical to calibrate the sensor with a prepared target for different real applications. Thus, to overcome the inconvenience during ITS operation, we propose a targetless extrinsic calibration method based on GPS for traffic radar. The global and accurate positioning information from high-precision GPS can improve the accuracy of calibration. The extrinsic calibration problem is then transformed into estimating the rigid transformation between the measurement sets of radar and GPS. The destination measurement set is obtained from the GPS mounted on the moving vehicle, and the source measurement set is obtained from the traffic radar mounted on the ITS infrastructure. By combining with the high-precision GPS, our traffic radar calibration method can promote the environmental perception fusion among each measurement points in the ITS, so as to build an accurate global coordinate system for the Digital Twin.

Please note that, for both target-based and targetless calibration methods, the complex target association problem must be addressed. In most studies, the extrinsic calibration is transformed into a correspondence-based registration (CBR) problem [19], [20], [21]. For instance, the correspondences are derived from the dedicated calibration target in target-based calibration approaches. In targetless approaches, researchers use environmental features sensed by both sensors to find the correspondences, such as geometric descriptors. Nevertheless, traffic radars can not provide any descriptive features such as edges and corners because of the measurement mechanism and

the limited resolution. The association of radar measurements with vehicles in image, or geometrical features from LiDAR point cloud is intractable. This association problem must be rethought from a different perspective, such as using the registration method to find correspondences between different sensors' measurements. Therefore, we consider that the above mentioned alignment of the measurement sets from radar and GPS is a simultaneous pose and correspondence registration (SPCR) problem [22], [23], [24], [25]. Different from the CBR problem, the correspondences in this problem are unknown, such that the correspondences and transformation need to be addressed simultaneously. Moreover, the objective functions in SPCR problem are usually non-convex due to the nonlinear rotation constraints [26]. Existing methods, such as ICP [22], CPD [24] and GMMReg [25], have been used to solve the SPCR problem. However, they are prone to delivering erroneous results (local optimum) during the iterative optimization process and are highly dependent on the initial estimation of transformation, i.e., initialization.

Recently, globally optimal methods have been proposed according to the Branch and Bound (BnB) paradigm [27], [28], [29]. The prominent features of BnB-based method are that *i)* it can find the globally optimal solutions with theoretical guarantee, *ii)* and it is independent of initialization. In this paper, we propose a robust globally optimal method to solve the SPCR problem for the targetless calibration, called Gaussian Mixture Robust Branch and Bound (GMRBnB). In detail, we first represent the measurement sets with the Gaussian Mixture Model (GMM) [25], [30] to counteract the influence of noise and outliers. Next, we construct the robust objective function using the closed-form solution of the statistical difference metric between two Gaussian mixtures. We then present a BnB-based optimization method with newly proposed relaxation bounds to find the globally optimal transformation. Notably, due to the inherent high computational cost drawback of BnB-based methods [31], our proposed method is only used for the offline calibration, which is admissible in real applications. We put more attention on the accuracy of the calibration, i.e., how to find the globally optimal solution.

Our contributions in this paper can be summarized as follows:

- 1) We propose a targetless calibration method for traffic radar to tackle the inconvenience during ITS operation. The combination of high-precision GPS on the moving vehicle and traffic radar on the ITS infrastructure enables accurate extrinsic calibration. Besides, there are no restrictions on the relative position of sensors, i.e., the relative angle and translation are arbitrary.
- 2) We propose a BnB-based globally optimal registration method to align the measurements of traffic radar and GPS in a simultaneous pose and correspondence registration manner. The GMRBnB algorithm searches the globally optimal solution in the domain of 2D rotation and translation. Therefore, our method can avoid failure by getting trapped in local optimal solutions in the case of large relative angles.

- 3) Extensive experiments demonstrate that the proposed method achieves accurate and robust performance on both synthetic and real-world data in contrast to the existing methods.

The rest of this paper is organized as follows: The next section addresses the related work in two directions and demonstrates the characteristics of our work in comparison to other approaches. Section III illustrates the problem formulation of the traffic radar extrinsic calibration. Section IV demonstrates the principle and details of our proposed method. Section V presents the experiments results with synthetic data and real-world data from our Providentia++ project. Finally, Section VI gives the conclusion.

II. RELATED WORK

In this section, we discuss the related work from the perspectives of: extrinsic calibration methods and optimization algorithms for registration, and then summarize the difference between current methods and ours.

A. Extrinsic Calibration Methods

In the past few decades, researchers have conducted a wide range of studies on the sensor extrinsic calibration to improve the perception accuracy of self-driving vehicles and ITSs. Generally, one of the requirements for extrinsic calibration is the reference feature, either from a dedicated target or another sensor's detection. This requirement divides the extrinsic calibration methods into two categories, target-based and targetless method.

Among the target-based radar calibration investigations, Natour et al. [32] established the radar-to-image correspondence by a dedicated target to implement the calibration between radar and camera. Peršić et al. [15] designed a triangular shaped calibration target for lidar and radar calibration. The calibration process includes reprojection error optimization and field-of-view optimization. Lee et al. [33] implemented the spatial and temporal calibration of automotive radar and lidar by the radar cross section (RCS) measurements from dedicated targets. Domhof et al. [34] proposed a novel extrinsic calibration tool for radar, camera and lidar based on a specialized target, and utilized three joint optimization configurations to perform both relative calibration and absolute calibration. In addition, Olutomilayo et al. [35] proposed a radar extrinsic calibration method based on corner reflector targets with known pose. They modeled the extrinsic calibration as a CBR problem and optimized it using the Kabsch algorithm. The advantages of target-based methods are accurate and easy to implement. However, target-based methods are impractical in our application, since the installation of dedicated targets on the highway is dangerous and infeasible.

Within targetless radar calibration investigations, Schöller et al. [36] proposed a data-driven targetless radar calibration approach based on deep learning to estimate the relative rotation angle, which can avoid the target association problem between camera and radar measurements. However, this approach only focuses on the rotational calibration and ignores the translational calibration. Izquierdo et al. [37]

proposed a targetless calibration method based on the high-definition (HD) map for multiple radars onboard a vehicle. The reference features are the static objects with specific categories and high RCS, such as street lights and traffic signs. But they assumed that the vehicle is able to localize in the HD map by using GNSS. Heng [38] proposed a targetless calibration method for multiple 3D lidars and 3D radars mounted on a vehicle. They first utilized the lidar data to build a 3D map of the environment, and then registered the radar scans with the 3D map. However, they also assumed that known vehicle poses are provided by a GNSS system. Wise et al. [39] utilized continuous-time velocity measurements to implement the extrinsic calibration of onboard 3D radar instead of 2D (planar) radar. This study is based on the ego-motion estimation of a moving vehicle, which is different from our application scenario. In general, above mentioned targetless methods are not suitable for our roadside static traffic radar calibration problem. They always need the help of additional prior information or a moving platform for the radar to associate targets. The correspondence is difficult to build directly in our practical situation due to the sparsity, the limited resolution, and the lack of descriptive features in traffic radar measurements. According to our practical requirements, the proposed targetless extrinsic calibration strategy, in combination with high-precision GPS, allow us to estimate the transformation between the coordinate systems of traffic radar and GPS without explicit target association.

B. Optimization Algorithms for Registration

Expectation-maximization (EM)-type methods are among the most classic approaches to solve the SPCR problem [22], which are iterative methods to find the maximum likelihood or maximum a posteriori (MAP) estimates of parameters. Within EM-type methods, ICP is the most representative. It iteratively corrects the transformation parameters to minimize the error metric, which usually is the sum of squared differences between the matched point sets. Subsequently, many variants [40], [41] were proposed to improve the performance of ICP. In recent years, researchers also represented the point set with GMM to improve the robustness to noise and outliers [23], [24], [25], [42]. These methods transform the registration problem into the probability distribution alignment problem, which seeks to maximize the similarity of two GMMs. Although all of these methods converge quickly to the optimal value when they have good initial estimations, they do not provide any performance guarantees. These methods are highly dependent on the initial estimations, and if the initial start point is not properly set, these algorithms tend to converge to the local minimum.

In addition to these local methods, there has been a great deal of research on solving the SPCR problem with global methods, such as stochastic methods [43], [44], feature-based alignment [45], [46] and BnB-based methods [26], [31], [47], [48], [49] in recent years. The former two are known as non-deterministic global optimization (NDGO) approaches, which can often succeed in terms of probability, but can not guarantee

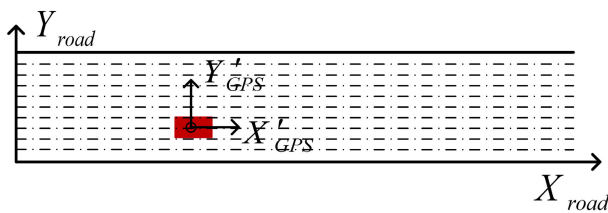


Fig. 3. The top view of GPS coordinate system.

to find a globally optimal solution. In particular, BnB-based methods are deterministic global optimization methods (DGO) [28], [50], which have theoretical guarantee of global optimality compared to the NDGO approaches. Among these existing BnB-based methods, Yang et al. [26] and Campbell and Petersson [47] addressed the 6 degrees of freedom (DOF) SPCR problem in a case of 3D point sets to 3D point sets, while Campbell et al. [31] and Liu et al. [48] addressed the 6DOF SPCR problem in a case of 3D point sets to 2D images. However, the extrinsic calibration in this paper is performed in the plane, so we particularly design the bounds functions of BnB to solve the 3DOF SPCR problem in a case of 2D measurement sets to 2D measurement sets. In this way, we eliminate the need for association between sensors' measurements.

In summary, the proposed targetless method can overcome the inconvenience during ITS operation to achieve accurate extrinsic calibration of the roadside traffic radar. To the best of our knowledge, our proposed method is the first-known approach to calibrate the extrinsic parameters in a simultaneous pose and correspondence registration manner. Additionally, our proposed registration method can search the globally optimal solution to avoid failure by falling into the local optimal solution, which is meaningful for safety-critical scenarios.

III. PROBLEM STATEMENT

A. ITS Coordinate System

The measurement of GPS is the pose of itself in the WGS-84 coordinate system, i.e., $(X_{GPS}, Y_{GPS}, Z_{GPS})$. It also is the trajectory of the moving vehicle with timestamps. In our study, the coordinate system of GPS measurements is converted to the same planar Universal Transverse Mercator (UTM) coordinate system as the ITS coordinate system (X_{road}, Y_{road}) , i.e., (X'_{GPS}, Y'_{GPS}) , as shown in Fig. 3. Further, radar detection of targets is all based on the same principle: low-frequency electromagnetic pulses are emitted from the radar antenna, and reflected back to the sensor from conductive targets in the environment [11]. We can obtain the bearing, distance and radial velocity of the target by measuring the time of flight and phase of the returned pulse. The roadside traffic radar performs projection on a horizontal plane with depth and azimuth of a detected target, and the projected point is denoted as $m_r(\alpha, r)$ in the 2D polar coordinate system, where α and r are azimuth and depth of the target respectively, as shown in Fig. 4. The height of the traffic radar H can be easily measured by a laser rangefinder, so that the measurements of traffic radar can be projected onto the same UTM plane with the

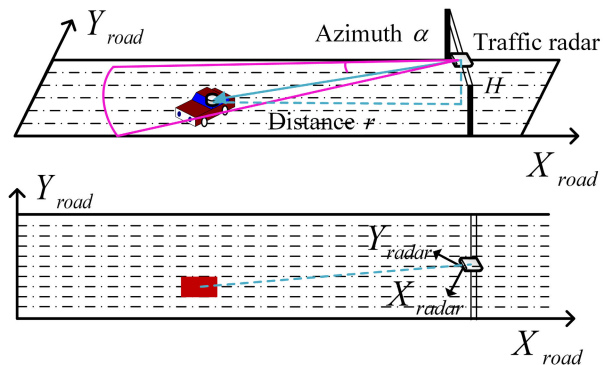


Fig. 4. The traffic radar coordinate system and its top view.

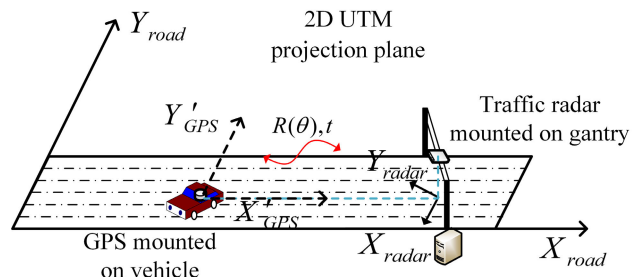


Fig. 5. The ITS coordinate system related to the extrinsic calibration.

coordinate system (X_{radar}, Y_{radar}) , as shown in Fig. 4. The overall ITS coordinate system is shown in Fig. 5. Regarding the traffic radar measurements, as we explained above, we can only acquire the pre-processed data of detected targets. Hence, under the geometric representation, the measurements in the measurement set are represented as discrete points in the coordinate system (X_{radar}, Y_{radar}) . Therefore, our targetless extrinsic calibration method is transformed into aligning the two measurement sets of radar and GPS in the 2D UTM projection plane, such that we can obtain the relative pose of traffic radar.

B. Measurement Set Registration Problem

Define the source and destination measurement sets $\mathcal{X} = \{X_1, X_2, \dots, X_m\}$ and $\mathcal{Y} = \{Y_1, Y_2, \dots, Y_n\}$, where $\mathcal{X}, \mathcal{Y} \subset \mathbb{R}^2$ represent the coordinates of measurements in radar and GPS frames, respectively. The problem is estimating the correspondence and 3DOF rigid transformation (with rotation angle $\theta \in [-\pi, \pi]$ and translation $\mathbf{t} \in \mathbb{R}^2$) between the two measurement sets, so that the transformed set \mathcal{X} is as close as possible to the set \mathcal{Y} . The L_2 residual between the transformed point X_i and point Y_j is defined as

$$e_{X_i, Y_j}(\theta, \mathbf{t}) = \|R(\theta)X_i + \mathbf{t} - Y_j\|_2 \quad (1)$$

where $R(\theta)$ is the rotation matrix, i.e.,

$$R(\theta) = \begin{bmatrix} \cos \theta & -\sin \theta \\ \sin \theta & \cos \theta \end{bmatrix} \quad (2)$$

Further, the residual between the transformed point X_i and set \mathcal{Y} is defined as

$$e_{X_i}(\theta, \mathbf{t}) = \min_{Y_j \in \mathcal{Y}} e_{X_i, Y_j}(\theta, \mathbf{t}) \quad (3)$$

which is to find the correspondence between point X_i and set \mathcal{Y} , i.e., find the closest point of X_i from the set \mathcal{Y} . Then the objective function to align the two measurement sets is given by

$$E(\theta, \mathbf{t}) = \sum_{i=1}^m e_{X_i}(\theta, \mathbf{t})^2 \quad (4)$$

The SPCR problem is trying to simultaneously find the optimal solution and correspondences that minimizes the objective function in Equation (4). If the real correspondences in Equation (3) are known, the rigid transformation in Equation (4) can be calculated in the closed-form by the optimizing algorithms such as the least squares optimization method based on Singular Value Decomposition (SVD). However, it is difficult to determine correspondences perfectly in practical applications. The solution of traditional local methods is prone to converge to the local minimum for the SPCR problem. On the other hand, the results are susceptible to the noise and outliers in measurement sets. In the following section, we utilize the GMM to construct the negative objective function for enhancing the robustness and propose a BnB-based method to find the globally optimal solution for this SPCR problem.

IV. METHOD

A. Gaussian Mixture Model and Similarity Measures

The representation of measurement sets with GMM is extensively employed to solve the registration problem. The main idea of this representation is mapping the discrete measurement sets to the continuous domain by probability density function, which is defined as a weighted sum of Gaussian density functions, i.e., $p(\mathbf{x}|\mathcal{G}) = \sum_{i=1}^k \omega_i \mathcal{N}(\mathbf{x}|\mu_i, \sigma_i^2)$. It is the probability density of observing a point \mathbf{x} given a GMM $\mathcal{G} = \{\omega_i, \mu_i, \sigma_i^2\}_{i=1}^k$, with mixture weights ω_i , means μ_i , variances σ_i^2 and the number of Gaussian components k , respectively. In summary, the benefits of GMM representation include: *i*) it uses a continuous probability density field for the representation of measurements and does not require partitioning and discretization of the space, *ii*) the covariance matrix in the GMM can better deal with the noise and outliers in the measurements, and *iii*) the correspondence update or closest point search is not performed during the optimization process.

Assuming no prior information, a simple construction method for GMM from the given measurement set is as follows: *i*) all Gaussian components have the same weights and covariance matrixes, *ii*) the mean of each component is the spatial coordinate of the corresponding measurement point, and *iii*) the number of Gaussian components and the measurement points are identical. Then the GMMs $\mathcal{G}_{\mathcal{X}} = \{\omega_i^{\mathcal{X}}, X_i, \sigma_{i\mathcal{X}}^2\}_{i=1}^m$ and $\mathcal{G}_{\mathcal{Y}} = \{\omega_j^{\mathcal{Y}}, Y_j, \sigma_{j\mathcal{Y}}^2\}_{j=1}^n$ are generated from the destination and source measurement sets \mathcal{X} and \mathcal{Y} respectively, as shown in Fig. 6. In this paper, the L_2 distance is employed as the statistical difference metric between two GMMs, since that the formulation can be expressed in closed-form [25]. We define the rigid transformation function $T(\mathcal{G}, \theta, \mathbf{t})$ to denote the rotation $\theta \in [-\pi, \pi]$ and translation

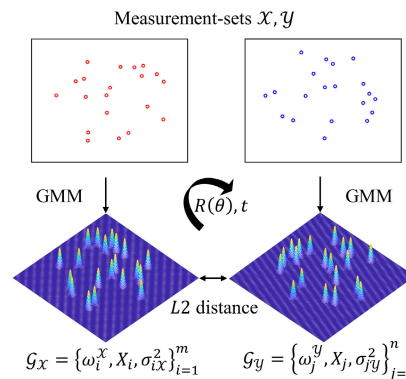


Fig. 6. The representation of measurement sets \mathcal{X} and \mathcal{Y} with GMMs $\mathcal{G}_{\mathcal{X}}$ and $\mathcal{G}_{\mathcal{Y}}$.

$\mathbf{t} \in \mathbb{R}^2$ for the GMM. The L_2 distance between two GMMs is defined as

$$D(\theta, \mathbf{t}) = \int_{\mathbb{R}^2} \left(p(\mathbf{x}|T(\mathcal{G}_{\mathcal{X}}, \theta, \mathbf{t})) - p(\mathbf{x}|\mathcal{G}_{\mathcal{Y}}) \right)^2 dx \quad (5)$$

The Equation (5) is then expanded as follows:

$$D(\theta, \mathbf{t}) = \int_{\mathbb{R}^2} \left[\left(p(\mathbf{x}|T(\mathcal{G}_{\mathcal{X}}, \theta, \mathbf{t})) \right)^2 + \left(p(\mathbf{x}|\mathcal{G}_{\mathcal{Y}}) \right)^2 - 2p(\mathbf{x}|T(\mathcal{G}_{\mathcal{X}}, \theta, \mathbf{t}))p(\mathbf{x}|\mathcal{G}_{\mathcal{Y}}) \right] dx \quad (6)$$

where the first term is invariant for any rigid transformation, the second term is independent of the rigid transformation, and the third term is relevant about the rigid transformation. However, the third term has a closed-form, derived by the following formula:

$$\begin{aligned} & \int_{\mathbb{R}^2} \mathcal{N}(\mathbf{x}|\mu_1, \sigma_1^2) \mathcal{N}(\mathbf{x}|\mu_2, \sigma_2^2) dx \\ &= \mathcal{N}(\mathbf{0}|\mu_1 - \mu_2, \sigma_1^2 + \sigma_2^2) \end{aligned} \quad (7)$$

Thus the negative GMM robust objective function over the L_2 distance is given by

$$\begin{aligned} G(\theta, \mathbf{t}) &= - \int_{\mathbb{R}^2} p(\mathbf{x}|T(\mathcal{G}_{\mathcal{X}}, \theta, \mathbf{t})) p(\mathbf{x}|\mathcal{G}_{\mathcal{Y}}) dx \\ &= - \sum_{i=1}^m \sum_{j=1}^n \omega_i^{\mathcal{X}} \omega_j^{\mathcal{Y}} \mathcal{N}(0|R(\theta)X_i + \mathbf{t} - Y_j, \sigma_{i\mathcal{X}}^2 + \sigma_{j\mathcal{Y}}^2) \\ &= - \sum_{i=1}^m \sum_{j=1}^n \frac{\omega_i^{\mathcal{X}} \omega_j^{\mathcal{Y}}}{N} \exp \left[- \frac{[e_{X_i, Y_j}(\theta, \mathbf{t})]^2}{2[\sigma_{i\mathcal{X}}^2 + \sigma_{j\mathcal{Y}}^2]} \right] \end{aligned} \quad (8)$$

where $e_{X_i, Y_j}(\theta, \mathbf{t})$ is the point-to-point L_2 residual in Equation (1) and N is the normalisation factor. We build a negative GMM objective function instead of traditional objective function in Equation (4), which displays statistical robustness to counteract the noise and outliers. Further, the most significant difference is that the GMM objective function does not need to find the closest corresponding point such as Equation (3). The function is the sum of the sums, not of the minima, so that the problem to be solved is simplified. In the next section, we derive the relaxation bounds for the minimum of this objective function.

B. BnB and Relaxation Bounds

BnB is a DGO framework for solving non-convex and NP-hard problems. It searches the entire solution domain to seek a globally optimal solution with theoretical guarantees. The BnB-based algorithm operates according to two principles, *i*) Branch: it recursively divides the search domain into smaller subboxes, and *ii*) Bound: it evaluates the lower and upper bounds on the optimal solution in each constrained subbox. Then the algorithm uses these bounds to prune the search domain and delete the subbox that it can prove do not contain the optimal solution. The algorithm converges when the lower and upper bounds on the optimal solution are tight enough, i.e., a predetermined threshold is achieved. The algorithm depends on efficient estimation of the lower and upper bounds of branches. Breadth-First Search (BFS) and Depth-First Search (DFS) have been employed to traverse the tree of subboxes [51]. The DFS strategy is recommended when no good heuristic is available for producing an initial estimation.

Define \mathcal{B} is the search domain and $B \in \mathcal{B}$ is the segmented subbox. Assume that functions $f_L(B)$ and $f_U(B)$ satisfy

$$f_L(B) \leq \min E(B) \leq f_U(B) \quad (9)$$

where $E(B)$ is the objective function, $f_L(B)$ is the lower bound function, and $f_U(B)$ is the upper bound function. It should be noted that the upper bound function can generally be chosen as the value obtained by substituting any value in the search domain or subboxes into the objective function. Besides, Equation (10) is the property of bounds functions that can guarantee the convergence of BnB-based algorithm, which is given by

$$\lim_{\sigma(B) \rightarrow 0} (f_L(B) - f_U(B)) = 0 \quad (10)$$

where $\sigma(B)$ is the diameter of box B . Equations (9) and (10) described above are necessary conditions to prove the bounds functions.

According to our registration problem, the parameterization of search domain is $\mathcal{B} = \{(\theta, \mathbf{t}) \in [-\pi, \pi] \times \mathbb{R}^2 \mid \mathbf{t}^- \leq \mathbf{t} \leq \mathbf{t}^+\}$. The rotation domain and translation domain are shown in Fig. 7. The next step is then to derive the lower and upper bound of the L_2 -based negative GMM objective function $G(\theta, \mathbf{t})$ within a domain \mathcal{B} , which is the most central part of the BnB-based method. In the objective function $G(\theta, \mathbf{t})$, all terms except for the point-to-point L_2 residual are easy to calculate, thus the focus is on bounding the point-to-point residual $e_{X_i, Y_j}(\theta, \mathbf{t})$.

Theorem 1 (Relaxation bounds of the objective function $G(\theta, \mathbf{t})$): For the 2D transformation domain $B = \{(\theta, \mathbf{t}) \mid \theta^- \leq \theta \leq \theta^+, \mathbf{t}^- \leq \mathbf{t} \leq \mathbf{t}^+\}$ centred at (θ_c, \mathbf{t}_c) , the relaxation upper bound $R_U(B)$ and lower bound $R_L(B)$ of the negative GMM robust objective function $G(\theta, \mathbf{t})$ for X_i, Y_j are

$$R_U(B) = - \sum_{i=1}^m \sum_{j=1}^n \frac{\omega_i \omega_j}{N} \exp \left[- \frac{[e_{X_i, Y_j}(\theta_c, \mathbf{t}_c)]^2}{2[\sigma_i^2 + \sigma_j^2]} \right] \quad (11)$$

$$R_L(B) = - \sum_{i=1}^m \sum_{j=1}^n \frac{\omega_i \omega_j}{N} \exp \left[- \frac{[e_{L, X_i, Y_j}(\theta, \mathbf{t})]^2}{2[\sigma_i^2 + \sigma_j^2]} \right] \quad (12)$$

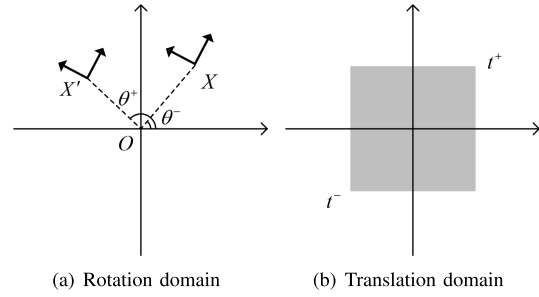


Fig. 7. Search domain parameterization for BnB. The rotation domain is the range of rotation angle, i.e., $[\theta^-, \theta^+]$. The translation is assumed to be a 2D rectangle $[\mathbf{t}^-, \mathbf{t}^+]^2$. The splitting policy is to divide from the center of each dimension of the domain, so there will be $2^3 = 8$ subboxes after one splitting.

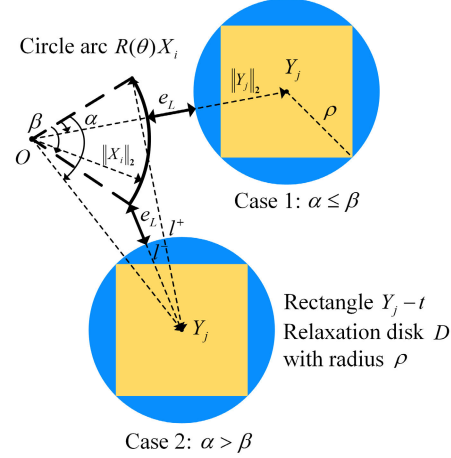


Fig. 8. The schematic of the relaxation lower bound function $R_L(B)$ with 2 cases, and e_L is the abbreviation of the lower bound of the point-to-point residual $e_{L, X_i, Y_j}(\theta, \mathbf{t})$.

where $e_{L, X_i, Y_j}(\theta, \mathbf{t})$ is the lower bound of the point-to-point L_2 residual $e_{X_i, Y_j}(\theta, \mathbf{t})$, and is given by

$$e_{L, X_i, Y_j}(\theta, \mathbf{t}) = \begin{cases} \max \left\{ \left| \|Y_j\|_2 - \|X_i\|_2 \right| - \rho, 0 \right\}, & \alpha \leq \beta \\ \max \left\{ \min\{l^-, l^+\} - \rho, 0 \right\}, & \alpha > \beta \end{cases} \quad (13)$$

where angles α, β are shown in Fig. 8, ρ is the radius of the translation relaxation disk, and $l^- = \|Y_j - R(\theta^-)X_i\|_2$, $l^+ = \|Y_j - R(\theta^+)X_i\|_2$.

Proof: To prove the effectiveness and validity of the relaxation lower bound $R_L(B)$ and upper bound $R_U(B)$ for the objective function $G(\theta, \mathbf{t})$, there are three issues that need to be addressed.

1) Observe that $\forall(\theta, \mathbf{t}) \in B$,

$$\min e_{X_i, Y_j}(\theta, \mathbf{t}) = \min \|R(\theta)X_i - (Y_j - \mathbf{t})\|_2 \quad (14)$$

This minimum can be denoted as the minimum distance between circle arc $\{R(\theta)X_i \mid \theta \in [\theta^-, \theta^+]\}$ and rectangle $\{\mathbf{x} \in \mathbb{R}^2 \mid Y_j - \mathbf{t}^+ \leq \mathbf{x} \leq Y_j - \mathbf{t}^-\}$ in any branch subbox $B = \{(\theta, \mathbf{t}) \mid \theta^- \leq \theta \leq \theta^+, \mathbf{t}^- \leq \mathbf{t} \leq \mathbf{t}^+\}$, and the radius of the arc is $\|X_i\|_2$. Then the rectangle domain can be relaxed to a disk shaped domain as shown in Fig. 8 and can be expressed by the following equation.

$$D = \{\mathbf{x} \in \mathbb{R}^2 \mid \|\mathbf{x} - Y_j\|_2^2 - \rho^2 \leq 0\} \quad (15)$$

where ρ is the radius of the relaxation disk, and $\rho = \|\mathbf{t}^+ - \mathbf{t}^-\|_2/2$. Obviously, the minimum distance between the circle arc and the rectangle is greater than or equal to the minimum distance between the circle arc and the relaxation disk, while both are greater than or equal to zero, that is,

$$\min e_{X_i, Y_j}(\theta, \mathbf{t}) \geq \min \|R(\theta)X_i - D\|_2 \geq 0 \quad (16)$$

Then the minimum distance between the circle arc and the relaxation disk is equal to the minimum distance between the circle arc and the center of the disk domain Y_j minus the radius of the relaxation disk ρ , which is

$$\min \|R(\theta)X_i - D\|_2 = \min \|R(\theta)X_i - Y_j\|_2 - \rho \quad (17)$$

The minimum distance between the circle arc and the center of the disk domain is an easy problem, that is, the minimum distance between the arc and the point. According to the different position relationships between the arc and the point, we divide it into two cases for consideration, as shown in Fig. 8. When the point lies within the rotation sector corresponding to the circle arc (Case 1), the minimum distance between the arc and the point is the difference between the two distances from the origin, which is $|\|Y_j\|_2 - \|X_i\|_2|$. When the point lies outside the rotation sector corresponding to the circle arc (Case 2), the minimum distance between the arc and the point is the minimum distance between the endpoints of the arc $R(\theta^-)X_i$, $R(\theta^+)X_i$ and the point, which is the minimum of $\{l^-, l^+\}$. Details are shown below,

$$\begin{aligned} & \min \|R(\theta)X_i - Y_j\|_2 - \rho \\ &= \begin{cases} \max \left\{ \|\|Y_j\|_2 - \|X_i\|_2\| - \rho, 0 \right\}, & \alpha \leq \beta \\ \max \left\{ \min\{l^-, l^+\} - \rho, 0 \right\}, & \alpha > \beta \end{cases} \end{aligned} \quad (18)$$

As for angles α and β , since the endpoints of the circle arc $R(\theta^-)X_i$, $R(\theta^+)X_i$ and the center of the disk domain Y_j are known, it is easy to compare these two angles. Define $e_{L, X_i, Y_j}(\theta, \mathbf{t}) = \min \|R(\theta)X_i - Y_j\|_2 - \rho$, then,

$$\min_{\forall(\theta, \mathbf{t}) \in B} e_{X_i, Y_j}(\theta, \mathbf{t}) \geq e_{L, X_i, Y_j}(\theta, \mathbf{t}) \quad (19)$$

By substitution into Equation (8),

$$\min_{\forall(\theta, \mathbf{t}) \in B} G(\theta, \mathbf{t}) \geq R_L(B) \quad (20)$$

Therefore, $R_L(B)$ is the lower bound of the objective function $G(\theta, \mathbf{t})$.

- 2) The point-to-point L_2 residual at a specific point within any subbox of the search domain is larger than the minimal residual within the search domain, that is

$$e_{X_i, Y_j}(\theta_c, \mathbf{t}_c) \geq \min_{\forall(\theta, \mathbf{t}) \in B} e_{X_i, Y_j}(\theta, \mathbf{t}) \quad (21)$$

Then substituting into Equation (8),

$$R_U(B) \geq \min_{\forall(\theta, \mathbf{t}) \in B} G(\theta, \mathbf{t}) \quad (22)$$

Therefore, $R_U(B)$ is the upper bound of the objective function $G(\theta, \mathbf{t})$.

- 3) When the search domain $B = \{(\theta, \mathbf{t}) | \theta^- \leq \theta \leq \theta^+, \mathbf{t}^- \leq \mathbf{t} \leq \mathbf{t}^+\}$ collapses to a single point (θ_0, \mathbf{t}_0) , then, $e_{X_i, Y_j}(\theta_0, \mathbf{t}_0) = e_{L, X_i, Y_j}(\theta_0, \mathbf{t}_0)$ and $R_L(\theta_0, \mathbf{t}_0) = R_U(\theta_0, \mathbf{t}_0)$, i.e.,

$$\lim_{\sigma(B) \rightarrow 0} (R_L(B) - R_U(B)) = 0 \quad (23)$$

The gap between upper bound and lower bound is equal to zero, and the convergence is proofed. ■

Algorithm 1 GMRBnB: An Algorithm for Globally Optimal Spatial Registration With Gaussian Mixture Model Representation

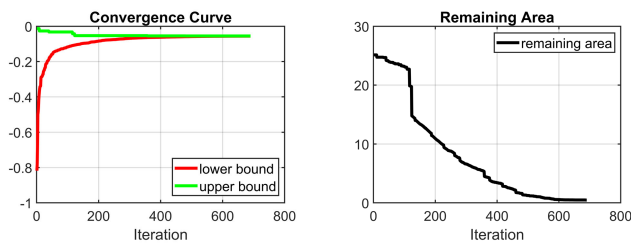
Require: Gaussian Mixture Models $\mathcal{G}_X, \mathcal{G}_Y$ with means X_i and Y_j respectively, weights ω , and variances σ^2 ; Solution domain B ; Convergence threshold ϵ

Ensure: ϵ -optimal solution $(\theta, \mathbf{t})^*$

- 1: Let ξ be the list of subboxes, initialize $B = B_0$, $\xi = \{B_0\}$, and normalize means X_i and Y_j
 - 2: Set $UB = R_U(\delta(B_0))$, and $(\theta, \mathbf{t})^* = \delta(B_0)$
 - 3: **while** The tolerance between global upper and lower bound is larger than the threshold ϵ such as $UB - LB > \epsilon$
do
 - 4: Select a subbox B with the minimum of lower bound, i.e., $B = \arg \min R_L(B_k)$, $B_k \in \xi$, and split it into eight sub-boxes $S(B) = \{B_1, \dots, B_8\}$
 - 5: Delete B from ξ , and add $\{B_1, \dots, B_8\}$ to ξ
 - 6: Update $LB = \min R_L(B_k)$, $B_k \in \xi$
 - 7: Update $UB = \min \left\{ UB, R_U(\delta(B_k)) \right\}$ with $B_k \in \xi$.
If $UB = R_U(\delta(B_k))$, set $(\theta, \mathbf{t})^* = \delta(B_k)$
 - 8: Delete B_k from ξ with $R_L(B_k) > UB$
 - 9: **end while**
-

C. The GMRBnB Algorithm

According to the relaxation bounds of the negative GMM robust objective function $G(\theta, \mathbf{t})$ in the last section, the GMRBnB algorithm is outlined in Algorithm 1. To simplify the calculation and speed up the algorithm, GMMs are assumed to have the same covariance matrix and weights. In practice, we can normalize the coordinates of measurement set so that the translation domain can be $[-1, 1]^2$, which can not only achieve a smaller box but also ensure that the domain covers every feasible translation, as shown in Line 1. Define function $\delta(B) \in B$ returns the center point of box B , and function $S(B) \in B$ divides the box B in half in each dimension of the solution domain. The exploration policy in Algorithm 1 is DFS. In detail, the search priority is inverse to the value of the lower bound as shown in Line 4, and the next branch to be divided is the branch with minimal lower bound. Line 5 is intended to delete the box that has been split. Line 6 is intended to update LB to the minimum of the current lower bound of all branches. Line 7 is intended to update UB to the minimum of the upper bound of all branches in all iterations.



(a) Bounds curve

(b) Remaining area

Fig. 9. Convergence curves of the proposed GMRbN algorithm.

The pruning policy is in Line 8, and the algorithm will prune the branch with lower bound larger than the global upper bound. After the algorithm converges, we obtain the ϵ -optimal solution without correspondences, i.e., only the transformation parameters (θ, \mathbf{t}) . This is because the GMM based objective function avoids solving the explicit target association problem, i.e., finding the closest corresponding point. In addition, the algorithm outputs the best-so-far solution in each iteration as shown in Line 7. Therefore, it can still provide best-guess transformation parameters when dealing with problems with limited running time, even if the upper and lower bounds are not fitted tightly enough.

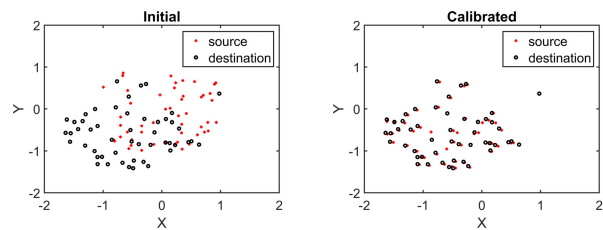
V. EXPERIMENTS

To demonstrate the performance and global optimality of the proposed method, we compare GMRbN with existing registration algorithms including ICP, CPD and GMMReg, using challenging synthetic and real data in this section. These algorithms are conducted in MATLAB 2019B, and all experiments are implemented on a laptop with Intel(R) Core(TM) i7-9750H CPU @ 2.60GHz and 16GB RAM.

A. Experimental Setup and Convergence

According to the property of the GMM objective function, the convergence range is influenced by the standard deviation σ of the Gaussian components, i.e., the width of the peak corresponding to the Gaussian distribution. Therefore, after some trying and comparing, the standard deviation σ of the Gaussian components is set to 0.1 in all experiments. What's more, there exists a normalization factor N in the objective function $G(\theta, \mathbf{t})$. Thus we set the convergence threshold for the GMRbN experiments as $\epsilon = 0.01$. In addition, to evaluate the accuracy and robustness, the translation error and rotation error are defined as $e_t = \|\mathbf{t}_{gt} - \mathbf{t}^*\|$ and $e_\theta = \|\theta_{gt} - \theta^*\|$ respectively, where \mathbf{t}_{gt} and θ_{gt} are motion ground truth, \mathbf{t}^* and θ^* are estimated solutions.

For a simple demonstration of the convergence for the proposed lower and upper bounds, we use a pair of synthetic measurement sets ($m = n = 20$) as input and obtain the convergence curves as shown in Fig. 9. It is obvious that the gap between the lower and upper bounds is converging to zero, and after several hundred iterations the proposed method can converge to the optimal solution. Moreover, the remaining area is rapidly decreasing.



(a) Initial measurement sets pair

(b) Calibrated measurement sets pair

Fig. 10. An example of measurement sets pair before and after calibration.

B. Control Experiments on Synthetic Data

This section is to illustrate the accuracy, robustness and global optimality of the proposed algorithm relative to the other three algorithms through three sets of control experiments. We use the synthetic data with different experimental conditions, which contain rotation angle, outlier rate, and noise level. In our experiments, we denote the false negatives and false positives in the correspondences as outliers uniformly.

1) *Data Generation*: Initially, the first measurement set is generated by creating m random points that are distributed in square $[-1, 1]^2$. Then the random rotation in $[-\pi, \pi]$ and random translation in $[-1, 1]^2$ are applied to this measurement set to obtain the corresponding transformed measurement set. They are the source measurement set and the destination measurement set, respectively. An example of a measurement sets pair before and after calibration is shown in Fig. 10. The simulation of the outliers is performed by randomly replacing some points in the transformed measurement set. The simulation of the noise is achieved by perturbing the measurement set with the noise from uniform distribution $U[-\delta_{noise}, \delta_{noise}]$.

Meanwhile, the average of the translation error e_t and rotation error e_θ for T trials represent the accuracy. The median runtime of T trials under each set of experimental conditions is also recorded in order to compare the efficiency and computational expense. Further, to demonstrate the global optimality of the proposed method, the success rate is defined as T^+/T , where T is the total number of trials under the same experimental conditions and T^+ is the number of successful cases satisfying $e_t < 0.1m$ and $e_\theta < 5^\circ$. As for the experimental conditions, the outlier rate is $\lambda = m_{outlier}/m$ where $m_{outlier}$ is the number of outliers and m is the total number of points in the measurement set. Further, the value of δ_{noise} is considered as the noise level.

2) *Deterministic Global Optimality*: In this section, we show the deterministic global optimality of the proposed GMRbN algorithm compared with ICP, CPD and GMMReg. In terms of the details of data generation, we rotate the source measurement set in the range of $[-180^\circ, 180^\circ]$ at 1° increments without translation to generate the destination measurement set. Each measurement sets pair has $m = n = 50$ points, and the outlier rate and noise level are $\lambda = 0$ and $\delta_{noise} = 0$ separately. For each rotation angle, we randomly generate the measurement sets pair 100 times and perform the related registration experiments with different algorithms. A case is considered successful when the rotation error satisfies $e_\theta < 5^\circ$. We perform the same experiments for ICP, CPD and GMMReg

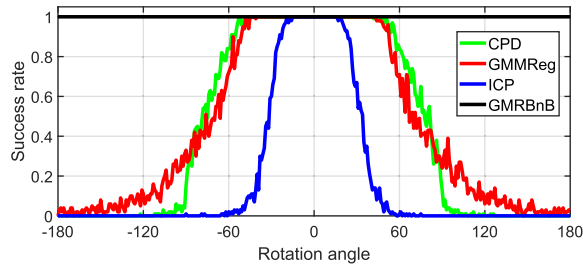


Fig. 11. Success rate of CPD, GMMReg, ICP and GMRBnB algorithms without translation.

and plot the success rate versus rotation angle as shown in Fig. 11.

As seen from Fig. 11, our proposed GMRBnB algorithm maintains a 100% success rate over the entire range of rotation angles, which represents the deterministic global optimality. However, the other algorithms only maintain a 100% success rate over a small range of rotation angles. The ICP algorithm has a 100% success rate only when rotation angle is in the range $[-15^\circ, 15^\circ]$, the CPD algorithm has a 100% success rate only in the range $[-48^\circ, 48^\circ]$, and the GMMReg algorithm has a 100% success rate only in the range $[-45^\circ, 45^\circ]$. When the range is exceeded, the success rate of these algorithms decreases rapidly. Moreover, when the rotation angle is close to about $\pm 60^\circ$, the success rate of ICP algorithm is close to zero, that for the CPD algorithm is about $\pm 105^\circ$, and that for the GMMReg algorithm is about $\pm 150^\circ$. The overall success rate of both the GMMReg and CPD algorithms are higher than that of the ICP algorithm, which indicates that the ICP algorithm is more easier to converge to a local optimum. In general, the GMRBnB algorithm has the deterministic global optimality and its convergence range is the whole rotation domain, which is much better than the other algorithms.

3) *Robustness to Noise and Outliers*: In this section, we compare the robustness to noise and outliers of each algorithm by challenging synthetic data experiments. The experimental conditions include different outlier rate and noise level. Firstly, the robustness of GMRBnB algorithm is tested in various outlier rates $\lambda = \{0, \dots, 0.5\}$ and then compared with other algorithms. The measurement sets pair with $m = n = 50$ points is generated in each experiment, and the noise level is $\delta_{noise} = 0.1$. Under each experimental settings, the experiment is repeated $T = 100$ times to verify the generality and global optimality. Further, the average rotation error, average translation error, median runtime and success rate are recorded and plotted in Fig. 12.

Secondly, the robustness of the GMRBnB algorithm is tested at different noise levels $\delta_{noise} = \{0, \dots, 0.12\}$. The measurement sets pair with the same $m = n = 50$ points is generated, and the outlier rate is $\lambda = 0.1$. This experiment is also repeated $T = 100$ times in each experimental setting to observe the global optimality. Besides, the average error, median runtime and success rate are plotted in Fig. 13.

From the results of all control experiments in this section, we summarize as follows:

- Firstly, as the outlier rate and the noise level increase, our proposed method always maintains a 100% success rate,

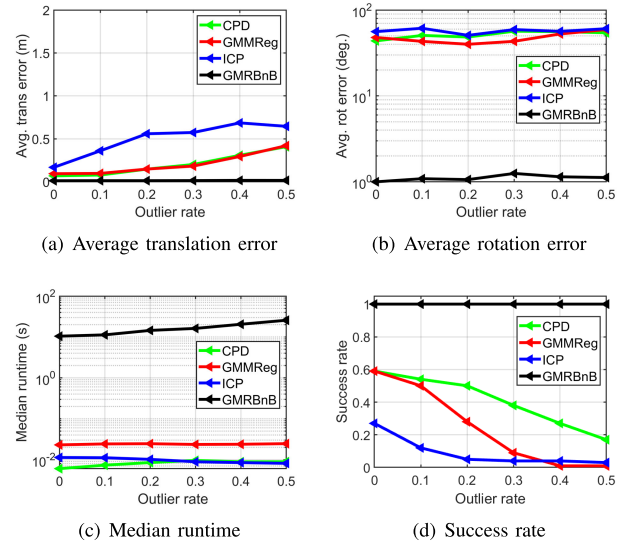


Fig. 12. Control experiments on synthetic data with different outlier rate.

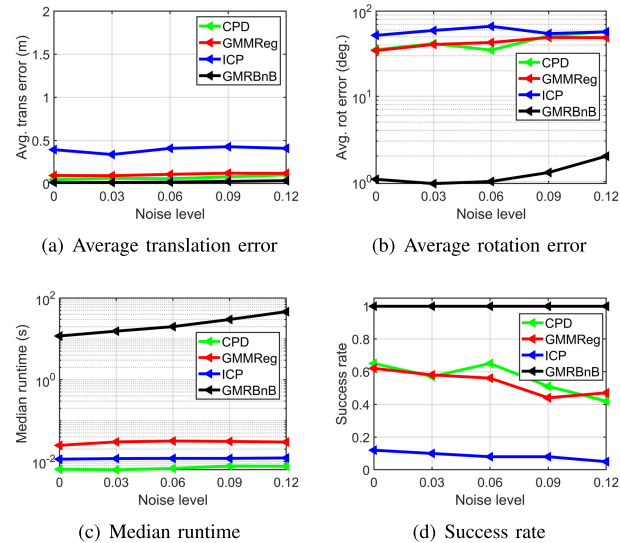


Fig. 13. Control experiments on synthetic data with different noise level.

which confirms the global optimality of the algorithm. Moreover, the robustness of the algorithm against outliers and noise is also demonstrated by the average error.

- Secondly, the average rotation errors of the ICP, CPD and GMMReg algorithms are much larger than that of the GMRBnB algorithm under all experimental conditions. According to the experiments in the previous section, it is clear that the rotation angle has a large effect on the success rate of these algorithms, while translation has a relatively small effect. Therefore, the average rotation errors of these algorithms become large in the arbitrarily repeated experiments. Besides, the average translation errors of the GMRBnB are all smaller than that of the ICP, CPD, and GMMReg algorithms. This also indicates that our proposed method can obtain better accuracy than other methods.
- Finally, our proposed method is higher than other algorithms in terms of computational cost. Because BnB-based methods search the whole solution domain



Fig. 14. This is our test car with high-precision RTK-GPS device (cm-level).

for the globally optimal solution, which is essential for safety-critical applications. But it is admissible for our offline calibration. Besides, the time required by proposed method increases with the increase in outlier rate or noise level due to the effects of outliers and noise.

C. Calibration Experiments on Real-World Data

In this section, we investigate the performance of GMRBnB on real-world data. These real data are collected by driving the test vehicle on parts of the German highway A9, which is the test field of ITS. Our test vehicle is equipped with a high precision RTK-GPS device as shown in Fig. 14. Multiple sensors are installed on the highway infrastructure, specifically on gantry bridges, overlooking a total of ten traffic lanes, as shown in Fig. 1. We repeatedly drive on the highway several times, each time passing in a different traffic lane and collecting detection data on the test vehicle from three traffic radars (Radar RA, RB and RC). These radars are installed in different locations and directions at two measurement points, but they have overlapped field of view. Notably, the radar measurements include missed detections, ghost detections, and multiple detections for trucks or buses due to measurement noise. In addition, the corresponding positioning information of the test vehicles is collected from the RTK-GPS device. The radar measurements are represented as the source measurement set with m measurement points, and the GPS measurements are represented as the destination measurement set with n measurement points.

1) *Manual Association and Ground Truth Acquisition:* In order to obtain the ground truth of these radars' poses, we calculate the closed-form solution of transformation using the method that manually establishes the target correspondence. Specifically, the timing clocks of traffic radar and GPS are unified to the ITS public clock under the form of unix timestamp first. Their measurements are then time-synchronized by a data interpolation method, since they have different sampling frequencies, which are 10Hz and 13Hz, respectively. Besides, the sensors' detection are transformed into the ITS coordinate system. Manual target association is then performed on the two sensors' measurements according to the unix timestamp, and the pair of measurement sets with the same size are obtained, i.e., $m = n$. Finally, the transformation matrix is calculated using the least squares optimization method based on SVD. The results are employed as the transformation ground truth

TABLE I
COMPARISON OF ROTATION ERROR AND TRANSLATION ERROR OF ALL ALGORITHMS FOR THREE RADARS

Methods		GMRBnB	ICP	GMMReg	CPD
Radar RA	$e_{\theta} (^{\circ})$	0.2419	-	-	-
	e_t (m)	0.2746	-	-	-
Radar RB	$e_{\theta} (^{\circ})$	0.0056	12.5305	12.8170	0.0688
	e_t (m)	0.9370	2.0060	1.7647	1.6873
Radar RC	$e_{\theta} (^{\circ})$	6.7084	7.0121	6.9147	7.0350
	e_t (m)	8.9213	9.5871	8.5321	10.1841

of follow-up experiments, as shown in Fig. 15(b) – Fig. 17(b). These are the closest values we can get to the real ground truth. It is apparent that the ground truth obtained even by manual association method does not enable a perfect alignment of the two measurement sets. Thus it is challenging to realize the traffic radar extrinsic calibration in this practical situation.

2) *Calibration Results:* In this section, the input data for the experiments are different from the input data for the least squares optimization method in previous section, which is the real measurement without manually established correspondence. The size of the measurement sets of the two sensors is different, because their sampling rates are similar. In the implementation, the input measurement sets are normalized such that the translation domain is set to be $[-1, 1]^2$. The targetless calibration is conducted offline. The accuracy and robustness of the calibration technology are our main focus. We then compare the calibration results of GMRBnB, ICP, GMMReg, and CPD for three radar's data with the manually obtained ground truth, as shown in Fig. 15 – Fig. 17. According to the ground truth, the rotation angles of the data corresponding to the three radars are 177.65° , 6.33° , 3.56° , respectively. As can be seen from Fig. 15, ICP, GMMReg, and CPD algorithms are failed to converge to the optimal solution. However, our proposed method can still obtain the globally optimal solution in the case of large relative angle. In Fig. 16 and Fig. 17, all methods including local methods converge to the correct result, because the relative rotation angle is close to zero degree. These results demonstrate that the proposed method can find the globally optimal solution with performance guarantees, while existing local methods are prone to wrong solutions (local optimum) in the case of large relative angle. The deterministic global optimality of the proposed method is verified in these experiments.

Meanwhile, we calculate the rotation error and translation error of all methods to compare the robustness, as shown in Table I. It is obvious that the rotation error and translation error of GMRBnB are almost the smallest with the data of all three radars. Even for the data of Radar RC, the translation error of GMRBnB is also competitive compared to the smallest value of GMMReg. Compared to other methods, the proposed method has a different formulation, in other words, a different objective function, which is the negative GMM objective function. Theoretically, each objective function has a different surface or shape, which leads to slightly different locations of the optimal solution corresponding to different objective functions [31]. The solution of proposed method

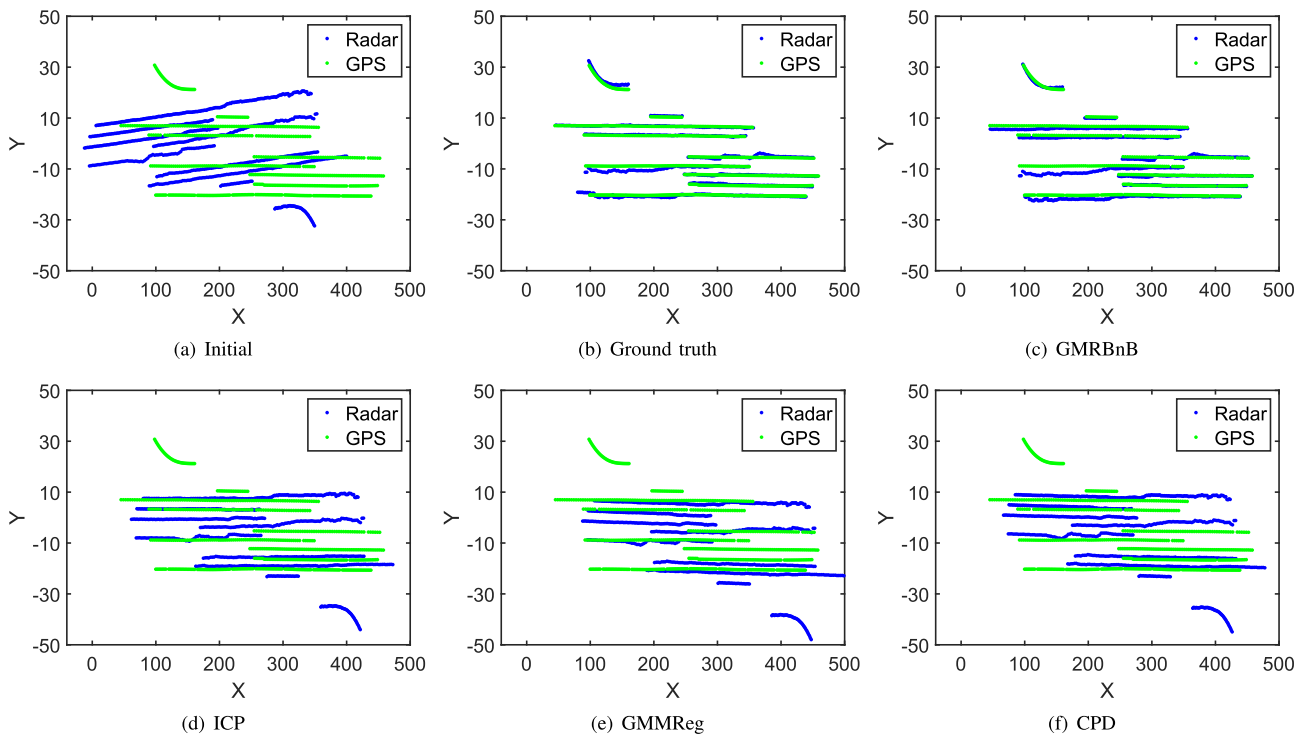


Fig. 15. The initial measurement sets of radar and GPS are $m = 851$ and $n = 637$, respectively. The calibration results of manual association, GMRBnB, ICP, GMMReg, and CPD for Radar RA are compared.

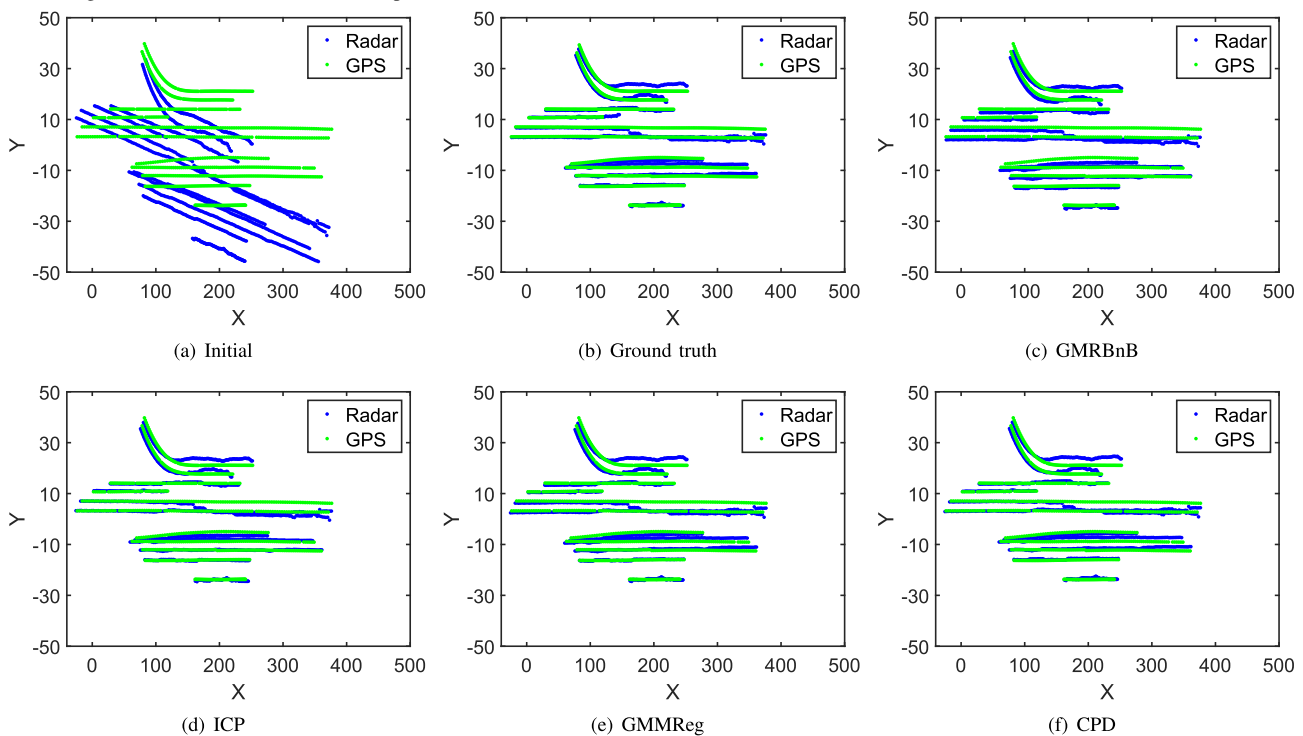


Fig. 16. The initial measurement sets of radar and GPS are $m = 1199$ and $n = 896$, respectively. The calibration results of manual association, GMRBnB, ICP, GMMReg, and CPD for Radar RB are compared.

is theoretically guaranteed to be optimal for our formulation. This is the reason that the translation error of our method is not minimal for Radar RC. On the other hand, the ground truth we used is manually obtained, and it even does not enable perfect alignment of the two measurement sets due to the large amount of noise and outliers inherent in the traffic radar measurements. Thus the errors of all methods for Radar RC

are relatively large. In summary, the results demonstrate that the proposed method is more robust to outliers and noise than existing local methods.

In addition, to further demonstrate the performance of the proposed calibration method applied to camera and traffic radar fusion in the ITS, we select a set of camera images and traffic radar detections from the real recorded data. After

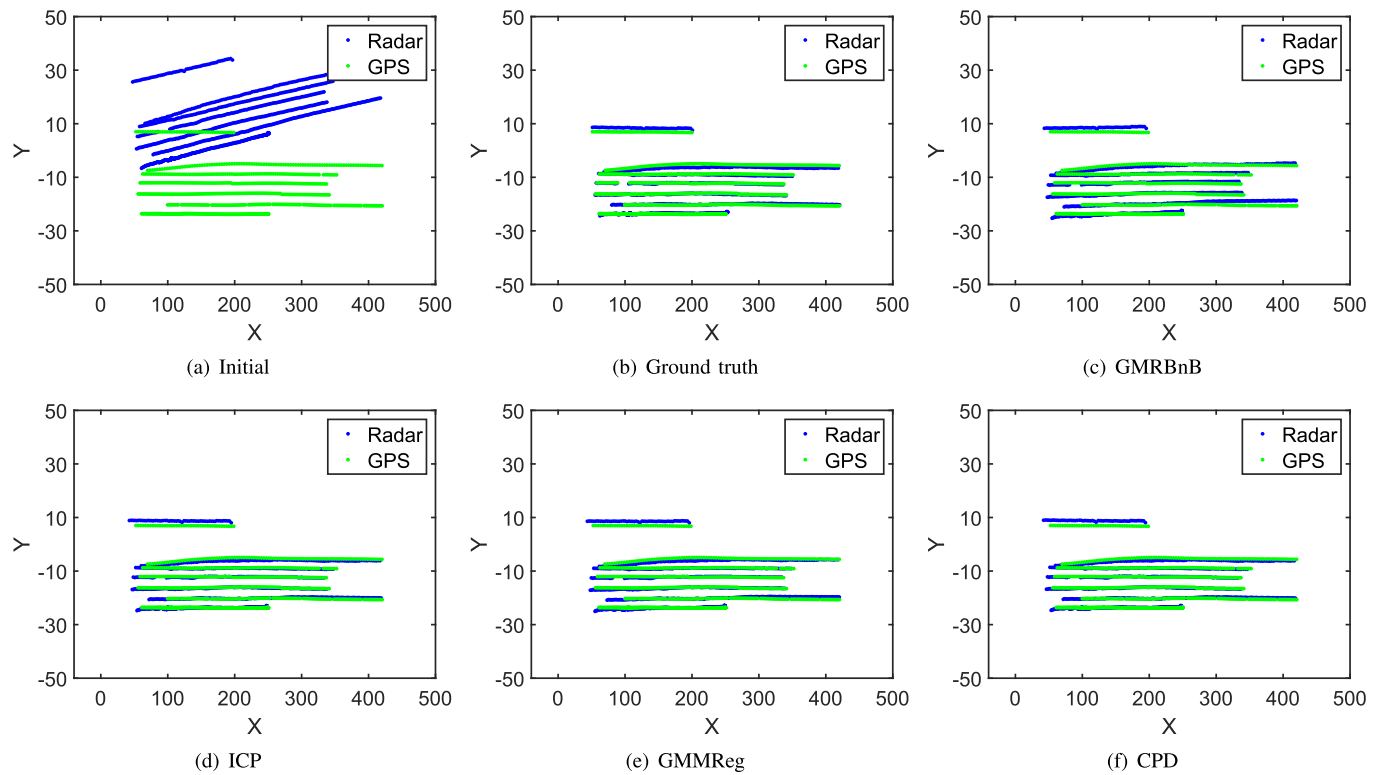


Fig. 17. The initial measurement sets of radar and GPS are $m = 1122$ and $n = 881$, respectively. The calibration results of manual association, GMRBnB, ICP, GMMReg, and CPD for Radar RC are compared.

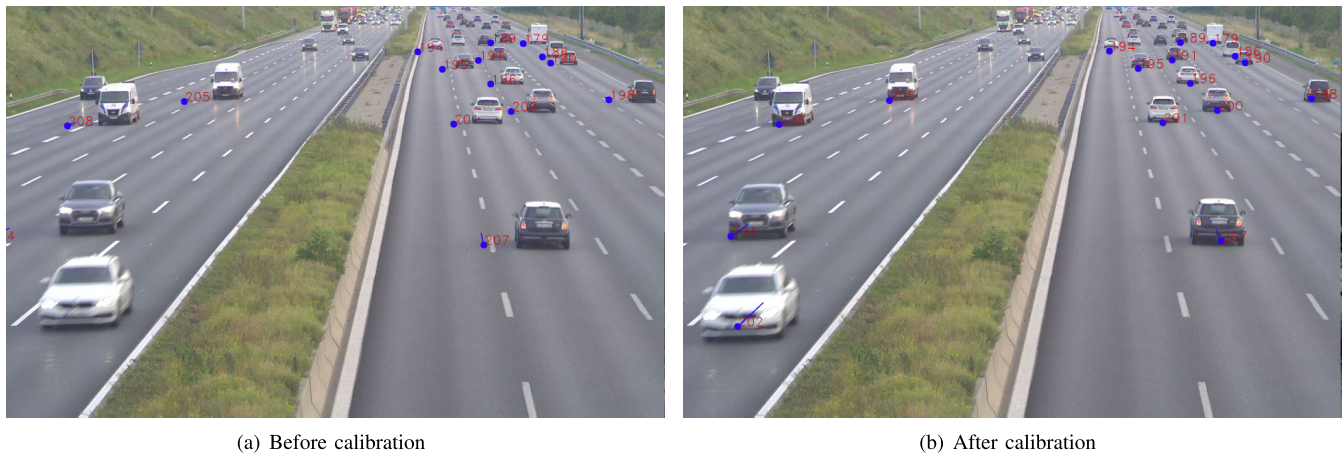


Fig. 18. After projecting the detection of Radar RC (blue points) onto the camera image, we compare the performance of the proposed calibration method before and after its application in a selected scenario.

projecting the radar measurements onto the camera image, we compare the performance of the proposed calibration method before and after its application, as shown in Fig. 18. The left image shows the initially erroneous calibration results, where the projected radar measurements do not align with the vehicles in the camera image. After implementing the proposed targetless extrinsic calibration, each detection is overlapped with the corresponding object in the camera image. Notably, a few measurement points are still not perfectly aligned with the vehicles in the image, which is caused by the noise in measurements. The results of traffic radar and camera fusion show that, our proposed method achieves precise and reliable extrinsic calibration of traffic radar, and

the calibration results are effective for camera and radar fusion.

VI. CONCLUSION

In order to tackle the inconvenience during ITS operation, we propose a targetless extrinsic calibration method for the traffic radar. This method does not require any dedicated target and is also safe and easy to implement. On the other hand, we use a simultaneous pose and correspondence registration method to address the difficult target association problem for radar measurements. Further, since existing registration methods are prone to converge to the local optimum and are overly dependent on the initialization, we propose a initialization-free

GMRbB algorithm to find the globally optimal solution with performance guarantees. We derive the novel relaxation upper and lower bound functions for the GMRbB algorithm. Then we conduct comparative experiments on challenging synthetic data to illustrate the theoretical performance of the proposed algorithm. Besides, we evaluate the performance of the proposed method on real-world data and validate the application in radar-camera fusion. Extensive experiments demonstrate that our proposed method not only can avoid failures due to getting trapped in local optimal solutions, but also is more accurate and robust than existing methods.

Nevertheless, there is still potential space for the improvement of the proposed method in some aspects. Currently, our method is only suitable for the offline calibration and also is not purely automatic for the ITS. Therefore, improving the efficiency and achieving automatic calibration is valuable. Because the sensors are susceptible to environmental disturbances such as vibration of the mounting bar due to high winds or displacement due to temperature changes. These perturbations lead to changes of the sensor's pose, hence the calibration parameters need to be automatically updated online. The second point is to model the system noise such as radar measurement noise, which not only allows the parameter settings be adapted to each specific device, but also increases the accuracy of the extrinsic calibration. Finally, joint spatio-temporal calibration is also a valuable extension direction of our approach.

REFERENCES

- [1] J. Zhang, F.-Y. Wang, K. Wang, W.-H. Lin, X. Xu, and C. Chen, "Data-driven intelligent transportation systems: A survey," *IEEE Trans. Intell. Transp. Syst.*, vol. 12, no. 4, pp. 1624–1639, Dec. 2011.
- [2] A. Krämmer, C. Schöller, D. Gulati, and A. Knoll, "Providentia—A large scale sensing system for the assistance of autonomous vehicles," in *Proc. Robot., Sci. Syst. (RSS), Workshop Scene Situation Understand. Auton. Driving*, 2019, pp. 1–12.
- [3] M. Dubska, A. Herout, R. Juránek, and J. Sochor, "Fully automatic roadside camera calibration for traffic surveillance," *IEEE Trans. Intell. Transp. Syst.*, vol. 16, no. 3, pp. 1162–1171, Jun. 2015.
- [4] Y. Du, B. Qin, C. Zhao, Y. Zhu, J. Cao, and Y. Ji, "A novel spatio-temporal synchronization method of roadside asynchronous MMW radar-camera for sensor fusion," *IEEE Trans. Intell. Transp. Syst.*, vol. 23, no. 11, pp. 22278–22289, Nov. 2022.
- [5] J. Beltrán, C. Guindel, A. de Escalera la, and F. García, "Automatic extrinsic calibration method for LiDAR and camera sensor setups," *IEEE Trans. Intell. Transp. Syst.*, vol. 23, no. 10, pp. 17677–17689, Oct. 2022.
- [6] B. Khaleghi, A. Khamis, F. O. Karray, and S. N. Razavi, "Multisensor data fusion: A review of the state-of-the-art," *Inf. Fusion*, vol. 14, no. 1, pp. 28–44, 2013.
- [7] R. O. Chavez-Garcia and O. Aycard, "Multiple sensor fusion and classification for moving object detection and tracking," *IEEE Trans. Intell. Transp. Syst.*, vol. 17, no. 2, pp. 525–534, Feb. 2016.
- [8] X. Wang, L. Xu, H. Sun, J. Xin, and N. Zheng, "On-road vehicle detection and tracking using MMW radar and monovision fusion," *IEEE Trans. Intell. Transp. Syst.*, vol. 17, no. 7, pp. 2075–2084, Jul. 2016.
- [9] E. Arnold, M. Dianati, R. de Temple, and S. Fallah, "Cooperative perception for 3D object detection in driving scenarios using infrastructure sensors," *IEEE Trans. Intell. Transp. Syst.*, vol. 23, no. 3, pp. 1852–1864, Mar. 2022.
- [10] G. Chen, H. Cao, J. Conrath, H. Tang, F. Rohrbein, and A. Knoll, "Event-based neuromorphic vision for autonomous driving: A paradigm shift for bio-inspired visual sensing and perception," *IEEE Signal Process. Mag.*, vol. 37, no. 4, pp. 34–49, Jul. 2020.
- [11] M. I. Skolnik, *Introduction to Radar Systems*. New York, NY, USA: McGraw-Hill, 1980.
- [12] T.-Y. Lim, S. A. Markowitz, and M. N. Do, "RaDiCaL: A synchronized FMCW radar, depth, IMU and RGB camera data dataset with low-level FMCW radar signals," *IEEE J. Sel. Topics Signal Process.*, vol. 15, no. 4, pp. 941–953, Jun. 2021.
- [13] J. Persic, I. Markovic, and I. Petrovic, "Extrinsic 6DoF calibration of 3D LiDAR and radar," in *Proc. Eur. Conf. Mobile Robots (ECMR)*, Sep. 2017, pp. 1–6.
- [14] J. Oh, K.-S. Kim, M. Park, and S. Kim, "A comparative study on camera-radar calibration methods," in *Proc. 15th Int. Conf. Control, Autom., Robot. Vis. (ICARCV)*, Nov. 2018, pp. 1057–1062.
- [15] J. Peršić, I. Marković, and I. Petrović, "Extrinsic 6DoF calibration of a radar–LiDAR–camera system enhanced by radar cross section estimates evaluation," *Robot. Auton. Syst.*, vol. 114, pp. 217–230, Apr. 2019.
- [16] J. Kang and N. L. Doh, "Automatic targetless camera–LiDAR calibration by aligning edge with Gaussian mixture model," *J. Field Robot.*, vol. 37, no. 1, pp. 158–179, Jan. 2020.
- [17] Q. Pentek, P. Kennel, T. Allouis, C. Fiorio, and O. Strauss, "A flexible targetless LiDAR–GNSS/INS–camera calibration method for UAV platforms," *ISPRS J. Photogramm. Remote Sens.*, vol. 166, pp. 294–307, Aug. 2020.
- [18] C. Yuan, X. Liu, X. Hong, and F. Zhang, "Pixel-level extrinsic self calibration of high resolution LiDAR and camera in targetless environments," *IEEE Robot. Autom. Lett.*, vol. 6, no. 4, pp. 7517–7524, Oct. 2021.
- [19] K. S. Arun, T. S. Huang, and S. D. Blostein, "Least-squares fitting of two 3-D point sets," *IEEE Trans. Pattern Anal. Mach. Intell.*, vol. PAMI-9, no. 5, pp. 698–700, Sep. 1987.
- [20] A. P. Bustos and T.-J. Chin, "Guaranteed outlier removal for point cloud registration with correspondences," *IEEE Trans. Pattern Anal. Mach. Intell.*, vol. 40, no. 12, pp. 2868–2882, Dec. 2018.
- [21] H. Yang, J. Shi, and L. Carlone, "TEASER: Fast and certifiable point cloud registration," *IEEE Trans. Robot.*, vol. 37, no. 2, pp. 314–333, Apr. 2021.
- [22] P. J. Besl and N. D. McKay, "Method for registration of 3-D shapes," *Proc. SPIE*, vol. 1611, pp. 586–606, Apr. 1992.
- [23] P. Biber and W. Strasser, "The normal distributions transform: A new approach to laser scan matching," in *Proc. IEEE/RSJ Int. Conf. Intell. Robots Syst. (IROS)*, vol. 3, Oct. 2003, pp. 2743–2748.
- [24] A. Myronenko and X. Song, "Point set registration: Coherent point drift," *IEEE Trans. Pattern Anal. Mach. Intell.*, vol. 32, no. 12, pp. 2262–2275, Dec. 2010.
- [25] B. Jian and B. C. Vemuri, "Robust point set registration using Gaussian mixture models," *IEEE Trans. Pattern Anal. Mach. Intell.*, vol. 33, no. 8, pp. 1633–1645, Aug. 2011.
- [26] J. Yang, H. Li, D. Campbell, and Y. Jia, "Go-ICP: A globally optimal solution to 3D ICP point-set registration," *IEEE Trans. Pattern Anal. Mach. Intell.*, vol. 38, no. 11, pp. 2241–2254, Nov. 2016.
- [27] J. Clausen, "Branch and bound algorithms-principles and examples," Dept. Comput. Sci., Univ. Copenhagen, Copenhagen, Denmark, Tech. Rep., 1999, pp. 1–30. [Online]. Available: https://janders.eecg.utoronto.ca/1387/readings/b_and_b.pdf
- [28] D. Scholz, *Deterministic Global Optimization: Geometric Branch-and-Bound Methods and Their Applications*, vol. 63. New York, NY, USA: Springer, 2011.
- [29] C. P. Tomazella and M. S. Nagano, "A comprehensive review of branch-and-bound algorithms: Guidelines and directions for further research on the flowshop scheduling problem," *Expert Syst. Appl.*, vol. 158, Nov. 2020, Art. no. 113556.
- [30] D. Reynolds, "Gaussian mixture models," *Encyclopedia Biometrics*, vol. 741, pp. 659–663, Jul. 2009.
- [31] D. Campbell, L. Petersson, L. Kneip, and H. Li, "Globally-optimal inlier set maximisation for camera pose and correspondence estimation," *IEEE Trans. Pattern Anal. Mach. Intell.*, vol. 42, no. 2, pp. 328–342, Feb. 2020.
- [32] G. E. Natour, O. A. Aider, R. Rouveure, F. Berry, and P. Faure, "Radar and vision sensors calibration for outdoor 3D reconstruction," in *Proc. IEEE Int. Conf. Robot. Autom. (ICRA)*, May 2015, pp. 2084–2089.
- [33] C.-L. Lee, Y.-H. Hsueh, C.-C. Wang, and W.-C. Lin, "Extrinsic and temporal calibration of automotive radar and 3D LiDAR," in *Proc. IEEE/RSJ Int. Conf. Intell. Robots Syst. (IROS)*, Oct. 2020, pp. 9976–9983.
- [34] J. Domhof, J. F. P. Kooij, and D. M. Gavrilu, "A joint extrinsic calibration tool for radar, camera and LiDAR," *IEEE Trans. Intell. Vehicles*, vol. 6, no. 3, pp. 571–582, Sep. 2021.

- [35] K. T. Olutomilayo, M. Bahramgiri, S. Nooshabadi, and D. R. Fuhrmann, "Extrinsic calibration of radar mount position and orientation with multiple target configurations," *IEEE Trans. Instrum. Meas.*, vol. 70, pp. 1–13, 2021.
- [36] C. Scholler et al., "Targetless rotational auto-calibration of radar and camera for intelligent transportation systems," in *Proc. IEEE Intell. Transp. Syst. Conf. (ITSC)*, Oct. 2019, pp. 3934–3941.
- [37] R. Izquierdo, I. Parra, D. Fernandez-Llorca, and M. A. Sotelo, "Multi-radar self-calibration method using high-definition digital maps for autonomous driving," in *Proc. 21st Int. Conf. Intell. Transp. Syst. (ITSC)*, Nov. 2018, pp. 2197–2202.
- [38] L. Heng, "Automatic targetless extrinsic calibration of multiple 3D LiDARs and radars," in *Proc. IEEE/RSJ Int. Conf. Intell. Robots Syst. (IROS)*, Oct. 2020, pp. 10669–10675.
- [39] E. Wise, J. Persic, C. Grebe, I. Petrovic, and J. Kelly, "A continuous-time approach for 3D radar-to-camera extrinsic calibration," in *Proc. IEEE Int. Conf. Robot. Autom. (ICRA)*, May 2021, pp. 13164–13170.
- [40] F. Pomerleau, F. Colas, R. Siegwart, and S. Magnenat, "Comparing ICP variants on real-world data sets," *Auto. Robots*, vol. 34, no. 3, pp. 133–148, 2013.
- [41] F. Pomerleau, F. Colas, and R. Siegwart, "A review of point cloud registration algorithms for mobile robotics," *Found. Trends Robot.*, vol. 4, no. 1, pp. 1–104, May 2015.
- [42] Y. Tsini and T. Kanade, "A correlation-based approach to robust point set registration," in *Proc. Eur. Conf. Comput. Vis. Cham, Switzerland: Springer*, 2004, pp. 558–569.
- [43] R. Sandhu, S. Dambreville, and A. Tannenbaum, "Point set registration via particle filtering and stochastic dynamics," *IEEE Trans. Pattern Anal. Mach. Intell.*, vol. 32, no. 8, pp. 1459–1473, Aug. 2010.
- [44] L. Li, M. Yang, C. Wang, and B. Wang, "Rigid point set registration based on cubature Kalman filter and its application in intelligent vehicles," *IEEE Trans. Intell. Transp. Syst.*, vol. 19, no. 6, pp. 1754–1765, Jun. 2018.
- [45] R. B. Rusu, N. Blodow, and M. Beetz, "Fast point feature histograms (FPFH) for 3D registration," in *Proc. IEEE Int. Conf. Robot. Autom.*, May 2009, pp. 3212–3217.
- [46] O. J. Woodford, M.-T. Pham, A. Maki, F. Perbet, and B. Stenger, "Demisting the Hough transform for 3D shape recognition and registration," *Int. J. Comput. Vis.*, vol. 106, no. 3, pp. 332–341, Feb. 2014.
- [47] D. Campbell and L. Petersson, "GOGMA: Globally-optimal Gaussian mixture alignment," in *Proc. IEEE Conf. Comput. Vis. Pattern Recognit. (CVPR)*, Jun. 2016, pp. 5685–5694.
- [48] Y. Liu, Y. Dong, Z. Song, and M. Wang, "2D–3D point set registration based on global rotation search," *IEEE Trans. Image Process.*, vol. 28, no. 5, pp. 2599–2613, Dec. 2018.
- [49] Y. Wang, Y. Liu, X. Li, C. Wang, M. Wang, and Z. Song, "Practical globally optimal consensus maximization by branch-and-bound based on interval arithmetic," *Pattern Recognit.*, vol. 115, Jul. 2021, Art. no. 107897.
- [50] C. A. Floudas, *Deterministic Global Optimization: Theory, Methods and Applications*, vol. 37. Cham, Switzerland: Springer, 2013.
- [51] K. Mehlhorn, P. Sanders, and P. Sanders, *Algorithms and Data Structures: The Basic Toolbox*, vol. 55. Cham, Switzerland: Springer, 2008.



Xinyi Li is currently pursuing the Ph.D. degree with the Chair of Robotics, Artificial Intelligence and Real-time Systems, TUM School of Computation, Information and Technology, Technical University of Munich. His research interests include multi-sensor calibration, point set registration, and pose estimation.



Yinlong Liu received the master's degree from the Digital Medical Research Center, School of Basic Medical Science, Fudan University, in 2018, and the Ph.D. degree from the Chair of Robotics, Artificial Intelligence and Real-time Systems, TUM School of Computation, Information and Technology, Technical University of Munich, in 2022. He is currently working at the University of Macau. His research interests include image-guided surgery and globally optimal solutions for geometric computer vision.



Venkatnarayanan Lakshminarasimhan is currently a Research Associate at the Chair of Robotics, Artificial Intelligence and Real-time Systems, TUM School of Computation, Information and Technology, Technical University of Munich. He is also the Technical Project Leader for the Providentia++ Research Project under which this work has been conducted.



Hu Cao received the M.Eng. degree in vehicle engineering from Hunan University, China, in 2019. He is currently pursuing the Ph.D. degree in computer science with the Chair of Robotics, Artificial Intelligence and Real-time Systems, Technical University of Munich, Munich, Germany. His research interests include computer vision, neuro-morphic engineering, robotics, and deep learning.



Feihu Zhang was born in Xi'an, China. He received the B.Sc. degree in automation and the M.Sc. degree in control theory and application from Xi'an Jiaotong University, Xi'an, in 2010, and the Ph.D. degree in informatics from the Technical University of Munich, Germany, in 2016. From 2014 to 2016, he was with the Data Fusion Group, fortiss GmbH. He is currently an Associate Professor with the School of Marine Science and Technology, Northwestern Polytechnical University, Xi'an. His main research interests include intelligent vehicle and robotic.



Alois Knoll (Fellow, IEEE) received the Diploma (M.Sc.) degree in electrical and communications engineering from the University of Stuttgart, Germany, in 1985, and the Ph.D. degree (summa cum laude) in computer science from the Technical University of Berlin, Germany, in 1988. He was on the faculty of the Computer Science Department, TU Berlin, until 1993. He joined the University of Bielefeld, as a Full Professor and the Director of the research group "Technical Informatics" until 2001. Since 2001, he has been a Professor at the Department of Informatics, Technical University of Munich (TUM). He was also on the board of directors of the Central Institute of Medical Technology, TUM (IMETUM). From 2004 to 2006, he was the Executive Director of the Institute of Computer Science, TUM. His research interests include cognitive, medical and sensor-based robotics, multi-agent systems, data fusion, adaptive systems, multimedia information retrieval, model-driven development of embedded systems with applications to automotive software and electric transportation, and simulation systems for robotics and traffic.